Medical Image Retrieval Based on Texture and Shape Feature Co-occurrence

Yixiao Zhou[a], Yan Huang[a], Haibin Ling[b] and Jingliang Peng[a]

[a]School of Computer Science and Technology, Shandong Provincial Key Laboratory of Software Engineering, Shandong University;

[b] Department of Computer and Information Sciences, Temple University

ABSTRACT

With the rapid development and wide application of medical imaging technology, explosive volumes of medical image data are produced every day all over the world. As such, it becomes increasingly challenging to manage and utilize such data effectively and efficiently. In particular, content-based medical image retrieval has been intensively researched in the past decade or so.

In this work, we propose a novel approach to content-based medical image retrieval utilizing the co-occurrence of both the texture and the shape features in contrast to most previous algorithms that use purely the texture or the shape feature. Specifically, we propose a novel form of representation for the co-occurrence of the texture and the shape features in an image, *i.e.*, the gray level and edge direction co-occurrence matrix (GLEDCOM). Based on GLEDCOM, we define eleven features forming a feature vector that is used to measure the similarity between images. As a result, it consistently yields outstanding performance on both images rich in texture (*e.g.*, image of brain) and images with dominant smooth regions and sharp edges (*e.g.*, image of bladder).

As demonstrated by experiments, the mean precision of retrieval with GLEDCOM algorithm outperforms a set of representative algorithms including the gray level co-occurrence matrix (GLCM) based, the Hu's seven moment invariants (HSMI) based, the uniformity estimation method (UEM) based and the the modified Zernike moments (MZM) based algorithms by 10%–20%.

Keywords: Content Based Medical Image Retrieval, Gray Level and Edge Direction Co-occurrence Matrix

1. INTRODUCTION

Rapid development of medical imaging technology, *e.g.*, Magnetic Resonance Imaging (MRI), Computed Tomography (CT) and x-ray mammography, has produced a huge number of medical images and created favorable conditions for medical diagnosis since the 1980s. Because of the explosively increasing number of images, it is often difficult to find valuable information from a large database of medical images.

With traditional text-based approaches to medical image retrieval, lots of effort is needed to label the image data, it is hard to extend the dimensionality of the labelling semantics, and the retrieval is often executed on only a coarse granularity. As such, content based image retrieval (CBIR) has been proposed to reduce the workload of data labelling and enhance the flexibility in semantics extension and query specification.

CBIR is a technique in which images are indexed by feature representations and the image retrieval is based upon those indexing features. The low level features are usually based on the color, the texture and/or the shape information contained in an image. In a CBIR system, the user poses a query (*e.g.*, by providing a sample image) and obtains images that are relevant to the query in terms of the indexing features.

Since many medical images do not contain color information, texture and shape features are often more important than color features in medical image retrieval. Prevalent algorithms utilize either texture or shape information in medical images, but they seldom make full use of both. As a result, their performance may largely depend on the specific characteristics of the medical images.

The goal of this work is to propose an algorithm that fully exploits both the texture and the shape information in medical images, such that it yields consistently satisfactory performance on medical images of generic characteristics.

Authors' email addresses: gangdelian@mail.sdu.edu.cn, yan.h@sdu.edu.cn, hbling@temple.edu and jingliap@gmail.com

Medical Imaging 2012: Computer-Aided Diagnosis, edited by Bram van Ginneken, Carol L. Novak,
Proc. of SPIE Vol. 8315, 83151Q · © 2012 SPIE · CCC code: 1605-7422/12/$18 · doi: 10.1117/12.911240

2. RELATED WORK

Medical images play an important role in medical training, surgical planning, patient diagnoses and so forth. Large numbers of medical images need to be managed in hospitals and other medical institutes and CBIR technology can help people do such a complex and huge task with high efficiency and low cost. In this section, we review a few medical image retrieval systems and some content based medical image retrieval schemes based on different features of the medical images.

Many systems related to medical image retrieval have been proposed including the Medical Image Management System (MIMS),[1,2] the Image Map[3] and The Web-based Medical Information Retrieval System (WebMIRS).[4] MIMS[1,2] is based on a synergy of several approaches for the retrieval of medical images. It can acquire significant information in the medical images and answer complex medical queries. MIMS extracts features concerning four aspects: storage of medical images, portability and independence concerns, simplicity of use and design and flexible query methods. The retrieval module in the MIMS is based on the interaction with users. The Image Map[3] is a method for indexing and similarity searching in image databases, whose main goal is fast query and secondary goal is supporting visualization and data-mining. WebMIRS[4] provides World Wide Web access to biomedical databases which we can access by standard SQL, by image content, or by a combination of the two.

The feature extraction algorithm plays a pivotal role in the CBIR System. Since many medical images do not contain color information, we focus on schemes that utilize the texture or the shape information in medical images.

The texture is an important attribute of images. Concerning the definition of texture and the quantification methods, there are three main types of approaches: co-occurrence matrices (statistical), Gabor filters (transform) and Markov Random Fields (model-based). The first known large-scale comparison of texture features was done by Ohanian and Dubest in 1992. They tested 16 co-occurrence features, 4 Markov Random Field (MRF) features, 16 Gabor filter features, and 4 fractal geometry features on 3200 32×32 sub-images and found that co-occurrence matrices performed the best.[5,6] Gray Level Co-occurrence Matrix (GLCM) is the most widely used and the most representative method in co-occurrence matrices methods. Therefore, in Section 4, we will compare GLEDCOM with GLCM to show the superiority of GLEDCOM in terms of the precision of retrieval.

The shape is another important attribute which can be used to describe the contents and targets of images. Concerning the definition of shape and the quantification methods, there are two main types of approaches: Moment Invariants[7] and Fourier Descriptor.[8] Hu's Seven Moment Invariants (HSMI) is a representative method in medical image retrieval based on shape features. Therefore, in Section 4, we will compare GLEDCOM with HSMI to show the superiority of GLEDCOM in terms of the precision of retrieval.

In recent years, new methods have been proposed for the purpose of medical image retrieval, which include Uniformity Estimation Method (UEM)[9] published in 2009 and Modified Zernike Moments (MZM)[10] published in 2011, respectively. The former is based on rotation invariant Local Binary Patterns(LBP) and the gradient orientation difference. It is a texture based method which can extract the uniformity information of brightness and structure in multiple directions from the images. The latter has the minimum geometric error and numerical integration error. It also uses the model of human recognition for observed objects in MZM and divides the image into several regions with different weights. In Section 4, we will compare GLEDCOM with them to show the superiority of GLEDCOM in terms of the precision of retrieval.

3. ALGORITHM DESCRIPTION

3.1 Overview

Edges play a very important role in describing the content of an image. Therefore, we focus on the geometric and the textural characteristics of the edge regions in a medical image for a concise and accurate description of the image. The former is depicted using edge directions while the latter using gray levels of the edge points, leading to the novel form of representation, *i.e.*, the gray level and edge direction co-occurrence matrix (GLEDCOM), for a medical image.

Based on GLEDCOM, we define eleven features forming a feature vector that is used to measure the similarity between images. For each medical image in the database, we compute its GLEDCOM-based feature vector in a preprocessing step. At run time, for a sample-based query posed by the user, we compute the GLEDCOM-based feature vector for the sample image, and compare it with those of the images in the database to obtain the images with high matching scores.

Specifically, the GLEDCOM-based feature vector extraction process consists of the following steps: (1) edge detection, (2) edge refinement, (3) edge direction estimation, (4) GLEDCOM construction and (5) feature vector computation. Given a medical image, the edge points are first identified through edge detection and refined for a cleaner result. Next, the direction of each edge point is estimated and the GLEDCOM for the image is constructed. Finally, the feature vector is computed based on the GLEDCOM, which will serve as the basis for comparison between images.

3.2 Edge Detection

Because Canny edge detection algorithm[11,12] has a good anti-noise performance and an accurate edge location capability, we use it to detect edges in the medical images. The algorithm is composed of three steps, *i.e.*, noise removal, gradient calculation and edge point determination.

3.2.1 Noise Removal

In the image edge detection process, the image noise has a great influence on the detection results. Noise may produce false edges and therefore eliminating image noise is one primary task of the edge detection.

In this work, we use the two-dimension zero-mean Gaussian function as the smoothing filter. Denoting the original image as $f(x, y)$, and the image after Gaussian filtering as $G(x, y)$, the Gaussian filtering process is expressed as $G(x, y) = f(x, y) * H(x, y)$ where $H(x, y) = \frac{1}{2\pi\sigma^2} e^{-(\frac{x^2+y^2}{2\sigma^2})}$. The parameter, σ, is the width of the Gaussian filter used to control the degree of smoothing.

In order for the Gaussian filter to work on a digital image, we need a Gaussian template that represents the discrete Gaussian function. We can get the Gaussian template of any size through establishing a $(2k+1)\times(2k+1)$ matrix that can be calculated as follows:

$$M(i, j) = \frac{1}{2\pi\sigma^2} e^{-\frac{(i-k-1)^2+(j-k-1)^2}{2\sigma^2}} \tag{1}$$

However, the Gaussian filter may also blur edges while eliminating noise. With the value of σ increasing, the band of the Gaussian filter will become wider, the extent of smoothing higher and the edges fuzzier. Experimentally, we have obtained the following Gaussian template by adjusting the value of σ, which has struck an optimal balance point between noise elimination and edge blurring for the images used in our experiments.

$$w = \frac{1}{16} \times \begin{vmatrix} 1 & 2 & 1 \\ 2 & 4 & 2 \\ 1 & 2 & 1 \end{vmatrix} \tag{2}$$

3.2.2 Gradient Calculation

We calculate the gradients at each pixel after the Gaussian filtering in four directions (the 0-degree, the 45-degree, the 90-degree, and the 135-degree directions) which we denote as D_0, D_{45}, D_{90} and D_{135}, respectively. The final gradient, D, of the central pixel is the maximum of D_0, D_{45}, D_{90} and D_{135} and the final gradient direction of the central pixel is the direction in which the gradient takes the maximum value.

Specifically, if we calculate the gradient at a pixel, we need to consider a 3×3 local neighborhood around that pixel. Denoting the gray level value of the central pixel as a_0 and the gray level values of the other pixels in the local neighborhood as a_i $(i = 1, 2, \ldots, 8)$, respectively, the configuration of the local neighborhood is illustrated in Fig. 1.

a_1	a_2	a_3
a_4	a_0	a_5
a_6	a_7	a_8

Figure 1. Local pixel neighborhood configuration.

The 0-degree gradient, the 45-degree gradient, the 90-degree gradient and the 135-degree gradient (denoted as D_0, D_{45}, D_{90} and D_{135}, respectively) at p_0 are calculated according to the following formulae.

$$\begin{aligned} D_0 &= a_6 + 2 \times a_7 + a_8 - a_1 - 2 \times a_2 - a_3 && (3)\\ D_{45} &= a_7 + 2 \times a_8 - 2 \times a_1 - a_2 && (4)\\ D_{90} &= -a_1 + a_3 - 2 \times a_4 + 2 \times a_5 - a_6 + a_8 && (5)\\ D_{135} &= a_2 + 2 \times a_3 - a_4 + a_5 - 2 \times a_6 - a_7 && (6)\\ & && (7) \end{aligned}$$

The final gradient, D, of the central pixel is calculated as

$$D = \max\{D_0, D_{45}, D_{90}, D_{135}\} \tag{8}$$

3.2.3 Edge Point Determination

A large gradient at a pixel means a dramatic change of gray values in its local neighborhood and often signifies an edge point on this pixel. Therefore, we can dichotomize the pixels of an image into two classes, namely edge points and non-edge points, by thresholding on the gradients:

$$f(x) = \begin{cases} 255, & \text{if} \quad Gr(x,y) \geq T; \\ 0, & \text{if} \quad Gr(x,y) < T. \end{cases} \tag{9}$$

Here T is the gradient threshold, $Gr(x,y)$ is the gradient image of the noise-removed image, $G(x,y)$, and $B(x,y)$ is the resultant binary image with a value of 255 standing for edge and a value of 0 standing for non-edge at each pixel.

The gradient threshold, T, is determined with an iterative optimization process as follows:

1. Calculate the initial gradient threshold T: $T = \frac{1}{2}(Gr_{max}+Gr_{min})$ where Gr_{max} and Gr_{min} is the maximum gradient and the minimum gradient in image $Gr(x,y)$, respectively.
2. Divide the pixels in the image $Gr(x,y)$ into two classes, R_1 and R_2, using T as the threshold.
3. Calculate the average gradient values, μ_1 and μ_2, in R_1 and R_2, respectively.
4. Calculate the new threshold T: $T = \frac{1}{2}(\mu_1 + \mu_2)$
5. Repeat Steps 2 to 4 until $|\mu_1 - \mu_2|$ is within a desired precision threshold or the number of iterations hits a maximum value specified by the user.

However, a straightforward single-thresholding approach can not guarantee the continuity of the edge points or will produce false edge points especially under the influence of noise.

In order to resolve these issues, a double-thresholding method is employed in the Canny edge detection algorithm. Specifically, a higher threshold is used to determine an initial set of edge points denoted as E, first. Edge points in E may be disjoint. Thereafter, starting from each pixel in E, we search along its gradient direction in its 3×3 neighborhood for new edge point (which will be added to E) using a lower threshold. By doing this, we expect to preserve the continuity of edge points with the final result set, E, of edge points. This double-thresholding algorithm consists of the following steps in turn:

1. Compute the global high threshold T_H using the method described above.
2. Calculate the global low threshold T_L: $T_L = aT_H$. We adopted $a = 0.4$ in our experiments which consistently yielded good results on our test images.
3. Each pixel (x, y) where $Gr(x, y) > T_H$ is an edge point.
4. Each pixel (v, w) where $\arctan \frac{w-y}{v-x}$ is the gradient direction of the pixel (x, y), $|v - x| \leq 1$, $|w - y| \leq 1$ and $Gr(x, y) > T_H$ is an edge point.

An example is shown in Fig. 2 to illustrate the effects of the single-thresholding and the double-thresholding methods for edge detection on the same bladder image as shown in Fig. 3(a). The result in Fig. 2(a) is obtained with the single-thresholding while the result in Fig. 2(b) with the double-thresholding method. Comparing Fig. 2(a) and Fig. 2(b), we see better preserved edge connectivity with the double-thresholding method.

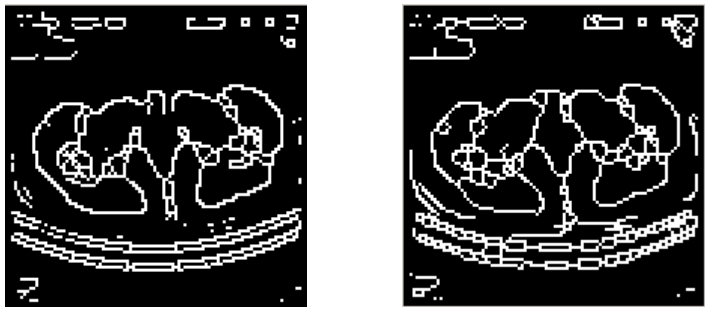

(a) (b)

Figure 2. Example results obtained with (a) the single-thresholding method and (b) the double-thresholding method for the bladder image as shown in Fig.3(a).

3.2.4 Edge Refinement

There usually is large redundancy in the edge point set obtained with the double-thresholding algorithm, as can be seen from Fig.3 where the original image and the detected edge points are shown in Fig.3(a) and Fig.3(b), respectively. We see that Fig.3(b) contains "thick" edges with redundant edge points detected. In order to remove the redundancy and highlight the shape characteristics of the objects, we perform a thinning process on the edge points obtained in Section 3.2. For that purpose, we use Zhang's fast parallel thinning algorithm[13] that is computationally efficient and preserves the connectivity of edge points. For the edge point set in Fig.3(b), the refined result after the thinning process is illustrated in Fig.3(c). The Zhang's thinning algorithm[13] is summarized as follows.

We denote the binary image after the double-thresholding process as $B(x, y)$, where a pixel value of 255 (0) signifies an edge (non-edge) point. The thinning process is conducted on this binary image to get a refined set of edge points. That is, we examine each pixel in $B(x, y)$ with a value of 255 and, based on the configuration of its local 3×3 neighborhood, determine whether this is a redundant edge point. Each redundant edge point is

(a) (b) (c)

Figure 3. For a bladder image in (a), the double thresholding process is performed to extract the edge point set as shown in (b), which is refined through a thinning process to obtain the final edge point set as shown in (c).

removed by setting the corresponding pixel value from 255 to 0 in $B(x, y)$. Specifically, using the same notation as given in Fig. 1, for each edge point with a pixel value $a_0 = 255$ in $B(x, y)$, we test if the following four conditions are met. If they are all met, this edge point is a redundant one and is removed.

1. $2 \leq f(a_0) \leq 6$
2. $g(a_0) = 1$
3. $a_2 \cdot a_4 \cdot a_5 = 0$ or $g(a_2) \neq 1$
4. $a_2 \cdot a_4 \cdot a_7 = 0$ or $g(a_4) \neq 1$

Here $f(a_0)$ is the number of edge points in the 3×3 local neighborhood not counting the central one and $g(a_0)$ is calculated as follows:

1. count = 0;
2. If $a_2 = 0$ and $a_1 = 255$, count = count + 1;
3. If $a_1 = 0$ and $a_4 = 255$, count = count + 1;
4. If $a_4 = 0$ and $a_6 = 255$, count = count + 1;
5. If $a_6 = 0$ and $a_7 = 255$, count = count + 1;
6. If $a_7 = 0$ and $a_8 = 255$, count = count + 1;
7. If $a_8 = 0$ and $a_5 = 255$, count = count + 1;
8. If $a_5 = 0$ and $a_3 = 255$, count = count + 1;
9. If $a_3 = 0$ and $a_2 = 255$, count = count + 1;
10. $g(a_0)$ = count;

The above redundant edge point removal process is iterated till no more edge points can be removed.

3.2.5 Edge Direction Estimation

At each edge point at (i, j) with $B(i, j) = 255$, we estimate the local direction of the edge. To that end, we first compute the 0-degree and the 90-degree derivatives, $p_0(i, j)$ and $p_{90}(i, j)$, using

$$P_0(i,j) = G(i,j+1) - G(i,j-1) \quad (10)$$

$$P_{90}(i,j) = G(i+1,j) - G(i-1,j) \quad (11)$$

where $G(x, y)$ is the image after Gaussian filtering.

The edge direction at the edge point (i, j) is then computed as

$$\theta(i,j) = \arctan \frac{P_0(i,j)}{P_{90}(i,j)} \quad (12)$$

.

3.2.6 GLEDCOM Construction

We uniformly quantize the gray values in the original image $f(x, y)$ to the range of $[1, K_z]$, and the direction values of the edge points as computed in Section 3.2.5 to the range of $[1, K_h]$. Then, the gray level and edge direction co-occurrence matrix (GLEDCOM) for the image $f(x, y)$ is defined as

$$\{H(i,j)/N | i = 1, 2, \ldots, K_z, j = 1, 2, \ldots, K_h\}$$

where $H(i,j)$ is the number of the edge pixels whose gray values are i and whose edge direction values are j and N is the total number of edge points.

It is worth noting that the GLEDCOM captures the joint shape and texture characteristics of the edge regions in the image, based on which we compute a set of features to statistically depict the content of the image.

3.2.7 Feature Vector Computation

After constructing the GLEDCOM, we compute a feature vector for statistical description of the content in the image. The feature vector is composed of eleven features that are computed in a way similar to that for the Gray Level Gradient Co-occurrence Matrix(GLGCM).[14,15] Specifically, we define the feature vector, T, as

$$T = [T_1, T_2, T_3, T_4, T_5, T_6, T_7, T_8, T_9, T_{10}, T_{11}]$$

where $T_1, T_2, \ldots, T_{11}$ are defined as follow in Table 1.

Table 1. Definition of features for GLEDCOM.

Symbol	Feature name	Formula
T_1	Small Edge Direction Dominance	$T_1 = [\sum_{i=1}^{K_z}\sum_{j=1}^{K_h}\frac{p(i,j)}{j^2}]$
T_2	Large Edge Direction Dominance	$T_2 = [\sum_{i=1}^{K_z}\sum_{j=1}^{K_h} p(i,j)\cdot j^2]$
T_3	Gray Asymmetry	$T_3 = \sum_{i=1}^{K_z}[\sum_{j=1}^{K_h} p(i,j)]^2$
T_4	Edge Direction Asymmetry	$T_4 = \sum_{j=1}^{K_h}[\sum_{i=1}^{K_z} p(i,j)]^2$
T_5	Energy	$T_5 = \sum_{i=1}^{K_z}\sum_{j=1}^{K_h}[p(i,j)]^2$
T_6	Correlation	$T_6 = \frac{1}{\partial_1\partial_2}\sum_{i=1}^{K_z}\sum_{j=1}^{K_h}(i-\mu_1)(j-\mu_2)p(i,j)$
T_7	Entropy	$T_7 = -\sum_{i=1}^{K_z}\sum_{j=1}^{K_h} p(i,j)\log_2 p(i,j)$
T_8	Gray Entropy	$T_8 = -\{\sum_{i=1}^{K_z}[\sum_{j=1}^{K_h} p(i,j)]\log_2[\sum_{j=1}^{K_h} p(i,j)]\}$
T_9	Edge Direction Entropy	$T_9 = -\{\sum_{j=1}^{K_h}[\sum_{i=1}^{K_z} p(i,j)]\log_2[\sum_{i=1}^{K_z} p(i,j)]\}$
T_{10}	Inertia	$T_{10} = \sum_{i=1}^{K_z}\sum_{j=1}^{K_h}(i-j)^2 p(i,j)$
T_{11}	Homogeneity	$T_{11} = \sum_{i=1}^{K_z}\sum_{j=1}^{K_h}\frac{1}{1+(i-j)^2}p(i,j)$
μ_1	Gray Mean	$\mu_1 = \sum_{i=1}^{K_z} i\cdot[\sum_{j=1}^{K_h} p(i,j)]$
μ_2	Edge Direction Mean	$\mu_2 = \sum_{i=1}^{K_h} j\cdot[\sum_{i=1}^{K_z} p(i,j)]$
σ_1	Gray Variance	$\partial_1 = \{\sum_{i=1}^{K_z}(i-\mu_1)^2[\sum_{j=1}^{K_h} p(i,j)]\}^{\frac{1}{2}}$
σ_2	Edge Direction Variance	$\partial_2 = \{\sum_{j=1}^{K_h}(j-\mu_2)^2[\sum_{i=1}^{K_z} p(i,j)]\}^{\frac{1}{2}}$

4. EXPERIMENTAL RESULTS

In our experiments, we use a medical image database consisting of 420 images including eight classes of images: bladder, nose pharynx, lung, femoral, brain, temporal bone, breast and chest images. Representative images from the database are shown in Fig. 4, each representing a specific class. Note that a representative bladder image is given in Fig. 3(a) already.

We first compare the GLEDCOM algorithm with the traditional algorithms: Gray Level Co-occurrence Matrix (GLCM) based on texture feature and Hu's Seven Moment Invariants (HSMI) based on shape feature. The experimental results are shown with histograms in Fig. 5 where the classes of images are marked on the bottom, different methods are color coded and the height of a bar represents the corresponding precision of retrieval. In Fig. 5, we can see that, except for the femoral images, GLEDCOM yields the highest precision among the three because it makes use of both the shape and the texture features in image description. The mean precision of GLEDCOM is 83.2% which is significantly higher than 71.2% of HSMI and 73.5% of GLCM.

We also compare the GLEDCOM algorithm with two latest algorithms: UEM and MZM. The experimental results are shown with histograms in Fig. 6 where the classes of images are marked on the bottom, different

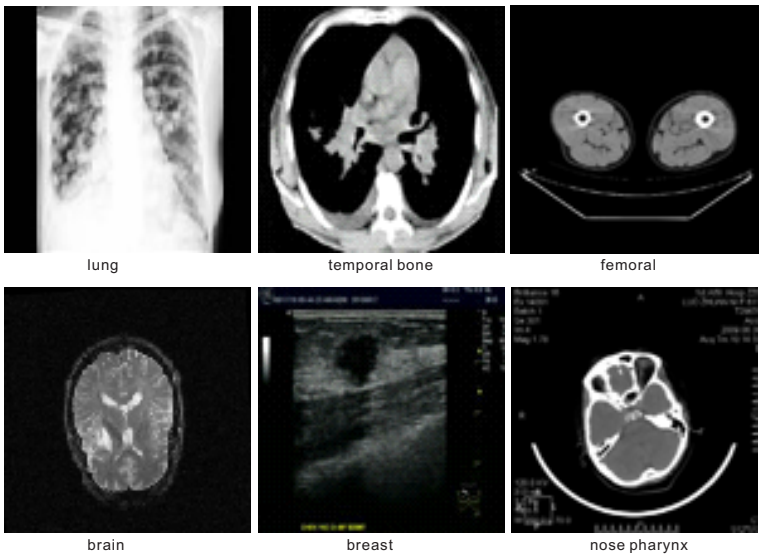

Figure 4. Samples from the medical image database that we use.

methods are color coded and the height of a bar represents the corresponding precision of retrieval. In Fig. 6, we can see that GLEDCOM yields the highest mean precision among the three. The mean precision of GLEDCOM is 83.2% which is significantly higher than 73.3% of UEM and 63.7% of MZM. Although in some classes GLEDCOM does not perform the best, the overall performance of GLEDCOM is superior to that of the other two methods because it makes use of both the shape and the texture features in image description.

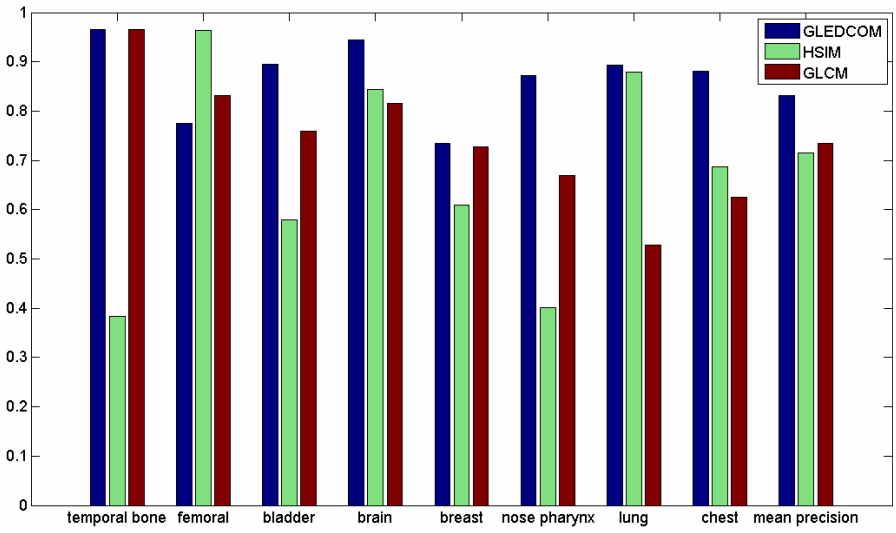

Figure 5. Precision of retrieval using GLEDCOM, HSMI and GLCM on eight classes of medical images.

5. CONCLUSION

In this work, we proposed a novel content-based medical image retrieval algorithm based on GLEDCOM, a novel form of representation for the co-occurrence of texture and shape features of the edge regions in an image. As experimentally demonstrated, it achieved a higher precision of retrieval on the average when compared with two traditional and two most recent state-of-the-art algorithms. As a future extension, we will continue to investigate

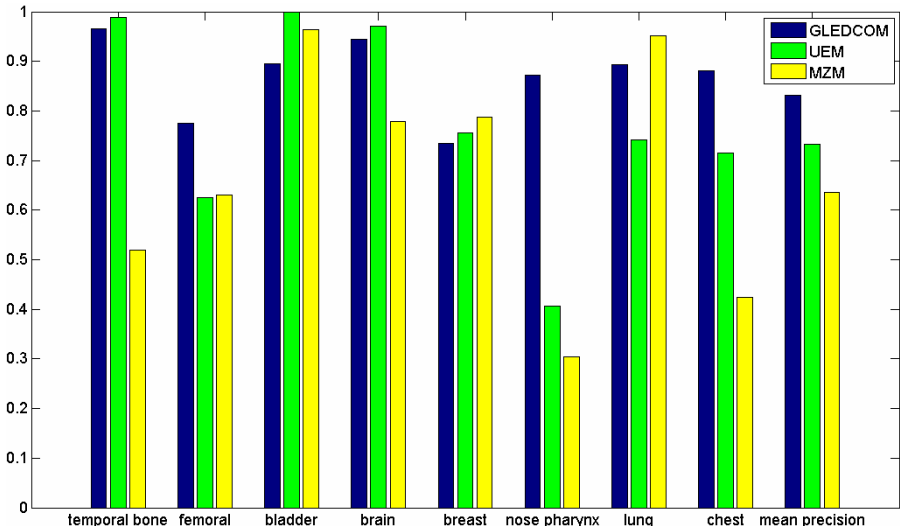

Figure 6. Precision of retrieval using GLEDCOM, UEM and MZM on eight classes of medical images.

techniques to reduce the gap between the results retrieved with the proposed algorithm and what the user expects based on a higher level of semantics.

6. ACKNOWLEDGEMENT

This work was supported in part by the National Natural Science Foundation of China (Grants No. 61070102, No. 61070103 and No. U1035004), the Program for New Century Excellent Talents in University (NCET) in China, Shandong Provincial Natural Science Foundation, China (Grant No. ZR2011FZ004), the Scientific Research Foundation for the Excellent Middle-Aged and Youth Scientists of Shandong Province of China (Grant No. BS2011DX017) and the US National Science Foundation (IIS-0916624 and IIS-1049032).

REFERENCES

[1] Chbeir, R., Amghar, Y., and Flory, A., "Mims: A prototype for medical image retrieval," in [*Proc. RIAO*], 846–861 (2000).

[2] Bach, J. R., Santanu, P., and Ramesh, J., "A visual information management system for the interactive retrieval of faces," *IEEE transactions on Knowledge and data engineering* **5**(4), 619–628 (1993).

[3] Petrakis, Euripidies, G. M., and Faloutsos, C., "Imagemap: An image indexing method based on spatial similarity," *IEEE transactions on Knowledge and data engineering* **14**(5), 979–987 (2002).

[4] Long, L., Pillemer, S., Lawrence, R., Goh, G., Neve, L., and Thoma, G., "Webmirs: Web-based medical information retrieval system," in [*Proceedings of SPIE Storage and Retrieval for Image and Video Databases VI*], *SPIE* **3312**.

[5] Lam, M., Disney, T., Pham, M., Raicu, D., Furst, J., and Susomboond, R., "Content-based image retrieval for pulmonary computed tomography nodule images," in [*SPIE Medical Imaging*],

[6] Ohanian, P. P. and Dubest, R. C., "Performance evaluation for four classes of textural features," *Pattern Recognition* **25**(8), 819–833 (1992).

[7] Hu, M. K., "Visual pattern recognition by moment invariants," *IRE Trans.on Information Theory* **8**(2), 179–187 (1962).

[8] Zhang, D. and Lu, G., "Shape-based image retrieval using generic fourier descriptor," *Signal Processing: Image Communication* **17**(10).

[9] Peng, S.-H., Kim, D.-H., Lee, S.-L., and Lim, M.-K., "Texture feature extraction based on a uniformity estimation method for local brightness and structure in chest ct images," *Computers in Biology and Medicine* **40**(11-12), 931–942 (2010).

[10] Ma, Z. M., Zhang, G., and Yan, L., "Shape feature descriptor using modified zernike moments," *Pattern Analysis & Applications* **14**(1), 9–22 (2011).
[11] Canny, J. F., "A computational approach to edge detection," *IEEE Trans. Pattern Analysis and Machine Intelligence* **8**.
[12] Ding, L. and Goshtasby, A., "On the canny edge detector," *Pattern Recognition* **34**(3), 721–725 (2001).
[13] T Y Zhang, C. Y. S., "A fast parallel algorithm for thinning digital patterns," *Communications of the ACM* **27**(3), 236–239 (1984).
[14] Lam, S.-C., "Texture feature extraction using gray level gradient based co-occurrence matrices," in [*IEEE International Conference on Systems, Man, and Cybernetics*],
[15] Key, T., "Image texture features of gas/liquid two-phase flow in horizontal pipes," in [*International Conference on Multiphase Flow*],